Supplementary Information

Enhanced energy storage density and efficiency in NBT-based MLCCs via a cooperative optimization of polarization and grain alignment

Yang Li[1], Ningbo Fan[2], Jie Wu[1], Bin Xu[2], Xuexin Li[1], Xuechen Liu[1], Yizhou Xiao[1], Dingwei Hou[1], Xinya Feng[1], Jinjing Zhang[1], Shujun Zhang[3*], Jinglei Li[1*] & Fei Li[1*]

1. Electronic Materials Research Laboratory, Key Laboratory of the Ministry of Education and International Center for Dielectric Research, School of Electronic and Information Engineering, Xi'an Jiaotong University, Xi'an, 710049, China.
2. Institute of Theoretical and Applied Physics, Jiangsu Key Laboratory of Thin Films, School of Physical Science and Technology, Soochow University, Suzhou 215006, China.
3. Institute of Superconducting and Electronic Materials, Faculty of Engineering and Information Science, University of Wollongong, Wollongong, NSW, Australia.

E-mail: shujun@uow.edu.au; lijinglei@xjtu.edu.cn; ful5@xjtu.edu.cn

Table S1 Space group and polarization of various types of defects from DFT calculations, including Mn (Mn^{4+}, Mn^{3+} and Mn^{2+}) and Ti^{3+} substitution of Ti^{4+}.

	Space group	Polarization ($\mu C \cdot cm^{-2}$)			
		P_x	P_y	P_z	$\|P\|$
$(Na_{0.5}Bi_{0.5})TiO_3$	*R3*	31.88	31.52	31.20	54.62
Ti^{3+}	*R3*	31.50	31.06	30.69	53.84
Mn^{4+}	*R3*	30.15	29.89	29.70	51.81
Mn^{3+}	*R3*	28.93	28.68	28.47	49.70
Mn^{2+}	*R3*	34.38	33.71	33.19	58.48

Table S2 DFT calculated displacement and polarization (Δu and *P*) for Ti^{4+} substitution with Ti^{3+}, Mn^{4+}, Mn^{3+} or Mn^{2+}, respectively, taking the high-symmetry cubic structure as reference.

	Δu_x	Δu_y	Δu_z	P_x	P_y	P_z
			$Na_{0.5}Bi_{0.5}TiO_3$			
A site (Na/Bi)	1.5164	1.5036	1.4912	15.36	15.24	15.08
B site (Ti/Mn)	0.7432	0.7372	0.7312	13.88	13.72	13.64
O site	-0.7624	-0.7564	-0.7500	2.64	2.56	2.48
tot	1.4972	1.4844	1.4724	31.88	31.52	31.20
			Ti^{3+}			
A site (Na/Bi)	1.4884	1.4738	1.4597	15.24	15.07	14.90
B site (Ti/Mn)	0.7576	0.7503	0.7429	13.71	13.55	13.40
O site	-0.7506	-0.7433	-0.7362	2.55	2.44	2.39
tot	1.4954	1.4808	1.4664	31.50	31.06	30.69
			Mn^{4+}			
A site (Na/Bi)	1.4175	1.4087	1.4002	15.01	14.91	14.81
B site (Ti/Mn)	0.6697	0.6655	0.6614	13.42	13.32	13.25
O site	-0.6030	-0.5996	-0.5957	1.72	1.66	1.64
tot	1.4842	1.4746	1.4659	30.15	29.89	29.70
			Mn^{3+}			
A site (Na/Bi)	1.4584	1.4481	1.4381	15.30	15.18	15.05
B site (Ti/Mn)	0.5941	0.5898	0.5857	11.83	11.75	11.66
O site	-0.5579	-0.5541	-0.5500	1.80	1.75	1.76
tot	1.4946	1.4838	1.4738	28.93	28.68	28.47
			Mn^{2+}			
A site (Na/Bi)	1.9213	1.8953	1.8700	17.30	17.05	16.76
B site (Ti/Mn)	0.8107	0.7998	0.7891	12.70	12.49	12.32
O site	-1.1879	-1.1714	-1.1560	4.38	4.17	4.11
tot	1.5441	1.5237	1.5031	34.38	33.71	33.19

Note: The displacement and polarization are in the units of Å and $\mu C \cdot cm^{-2}$, respectively.

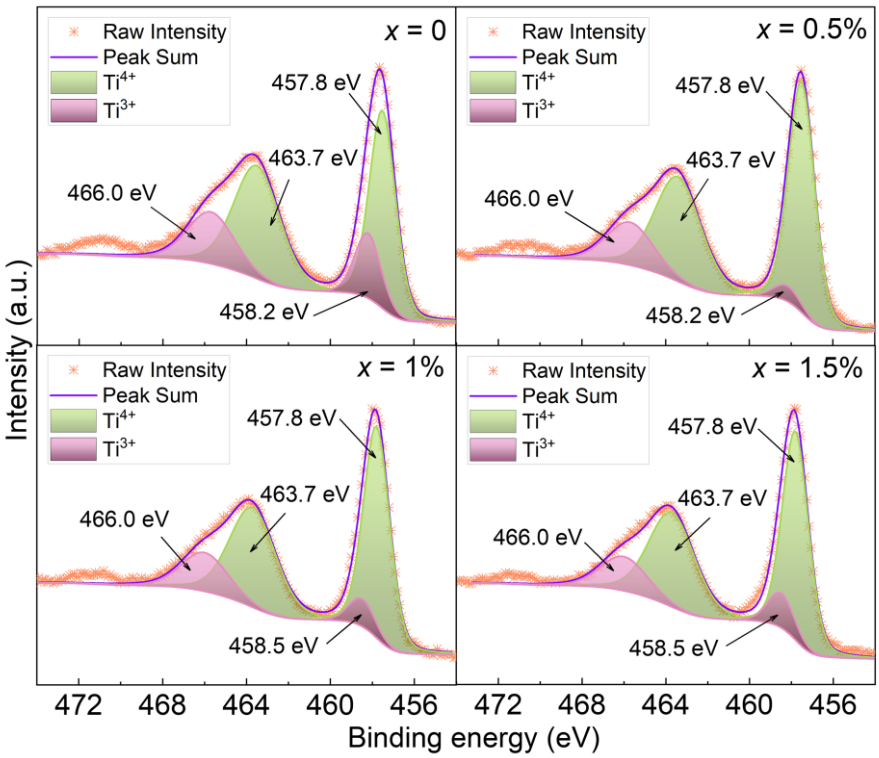

Figure S1 XPS of Ti in NBT-SBT-*x*Mn ceramics

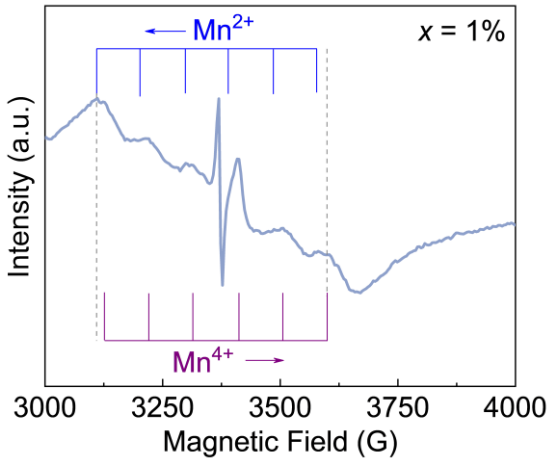

Figure S2 EPR of Ti in NBT-SBT-1 mol% Mn ceramic

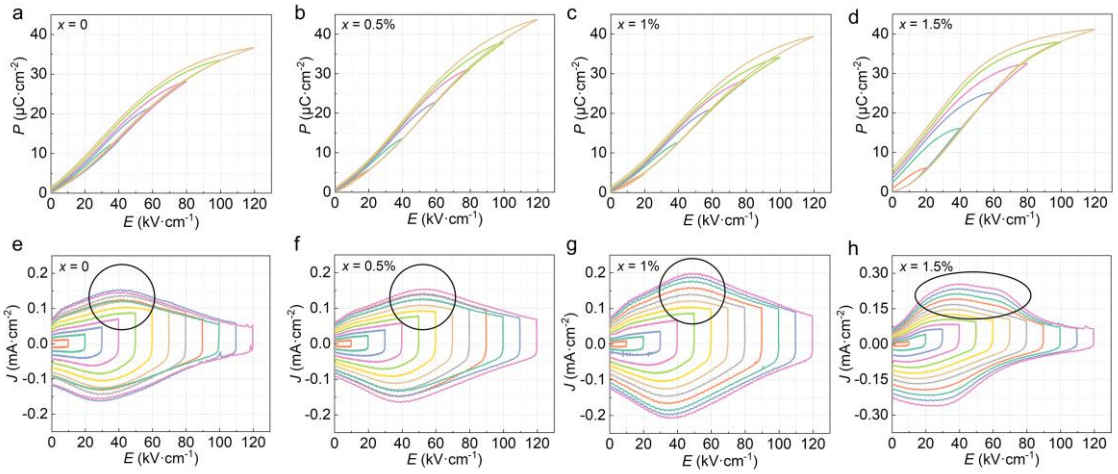

Figure S3 *P*-*E* loops and *J*-*E* curves of NBT-SBT-*x*Mn ceramics

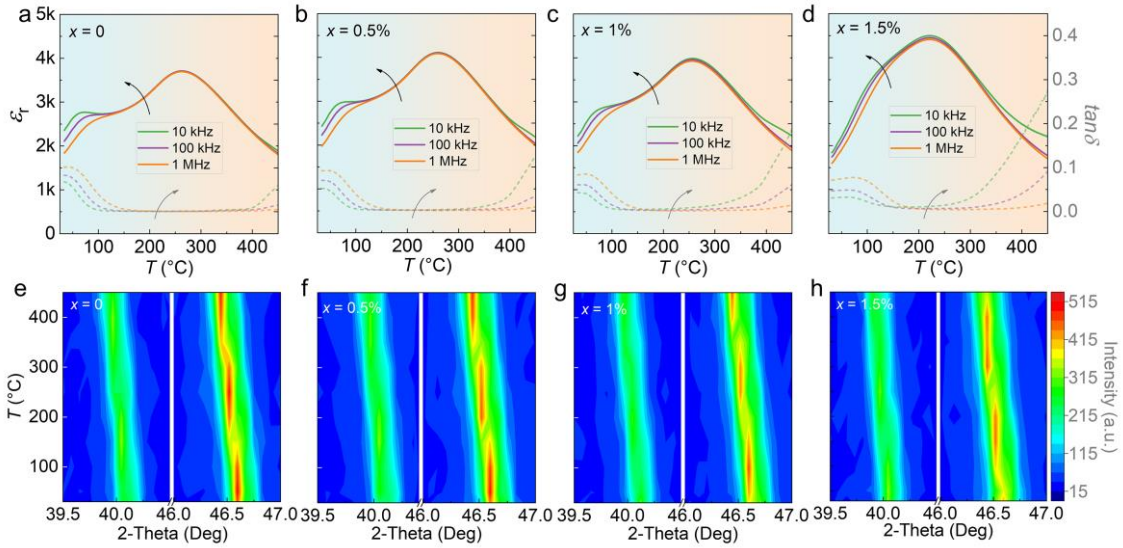

Figure S4 Dielectric temperature spectra and XRD at different temperatures of NBT-SBT-*x*Mn ceramics

When the Mn content ranges from 0 to 1 mol%, the dielectric constant exhibits similar temperature-dependent behaviors characterized by two prominent phase transition peaks, denoted as T_1 occurring around 70 °C and T_2 near 250 °C. The T_1 peak associating with rhombic-tetragonal phase transition demonstrates a significant frequency dispersion, indicative of the relaxor behavior, while the T_2 peak corresponds to the tetragonal-cubic phase transition.

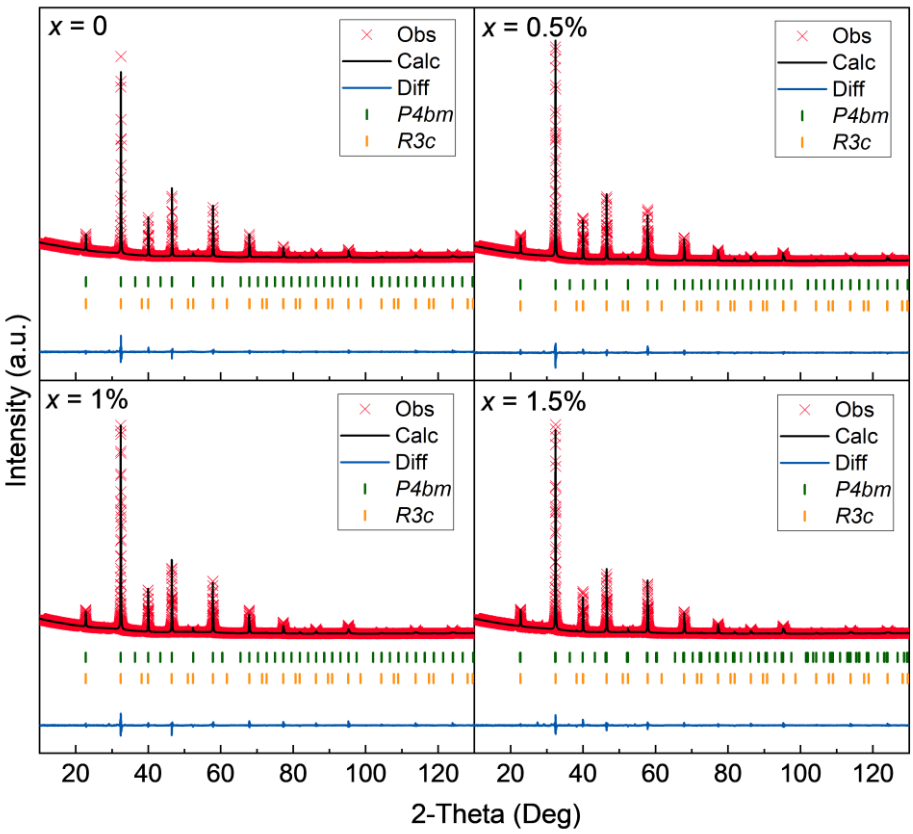

Figure S5 Rietveld refinement of XRD for NBT-SBT-*x*Mn ceramics

Table S3 Rietveld refinement parameters

Sample	Density (g cm^{-3})	Space group	Phase content (%)	*a* (Å)	*b* (Å)	*c* (Å)	*α* (°)	*β* (°)	*γ* (°)	R_w (%)	χ^2 (%)
x = 0	5.794020	*P4bm*	24.9	5.51965(9)	5.51965(9)	3.90059(7)	90	90	90	4.176	4.09
		R3c	75.1	5.51714(4)	5.51714(4)	13.5166(7)	90	90	120		
x = 0.5%	5.806849	*P4bm*	28.3	5.51717(3)	5.51717(3)	3.90036(2)	90	90	90	4.041	4.03
		R3c	71.7	5.51707(4)	5.51707(4)	13.5187(3)	90	90	120		
x = 1%	5.891710	*P4bm*	31.0	5.51530(9)	5.51530(9)	3.89785(9)	90	90	90	4.709	5.5
		R3c	69.0	5.51653(2)	5.51653(2)	13.5132(3)	90	90	120		
x = 1.5%	5.819680	*P4bm*	15.2	5.5156(0)	5.5156(0)	3.92230(3)	90	90	90	5.185	6.64
		R3c	84.8	5.51478(7)	5.51478(7)	13.5108(1)	90	90	120		

The refined parameters obtained from Rietveld refinement are summarized in Tab. S3, showcasing a tetragonal phase with *P4bm* space group and a rhombic phase with *R3c* space group coexist in all compositions. It should be noted that the Rietveld refinement of the 1.5 mol% Mn component considers only its perovskite main crystal phase, excluding the structure of its second phase. Incremental Mn content up to 1 mol% leads to a slight increase in tetragonal phase content. Conversely, with Mn content increasing to 1.5 mol%, the content of the tetragonal phase experiences a significant decrease, affirming the narrowing of the temperature range associated with the tetragonal phase mentioned in the main text.

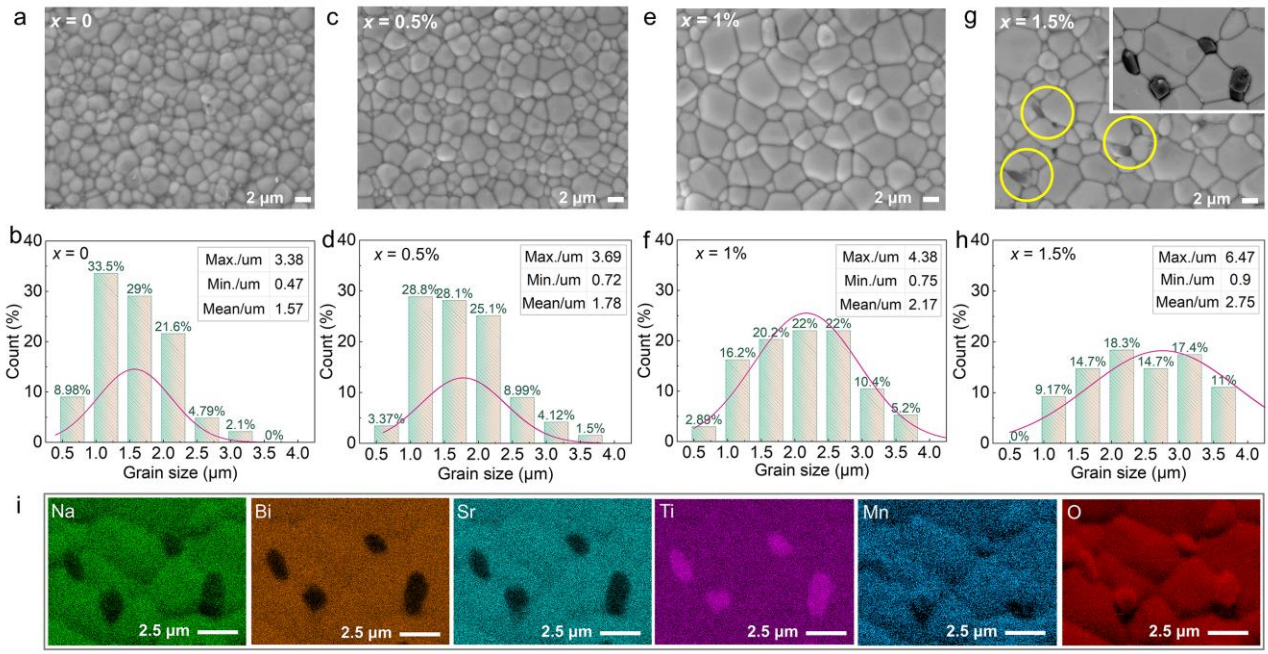

Figure S6 Surface morphology, grain size distribution of NBT-SBT-*x*Mn ceramics and EDS of *x* = 1.5 mol% ceramics

Surface microstructure characterization results presented reveal abnormally shaped second-phase grains on the surface of the 1.5 mol% Mn component. The energy dispersive spectroscopy

(EDS) characterization results corroborate the high amount of Mn, Ti, and O elements within these second-phase grains, consistent with the XRD characterization results.

Table S4 Raman peak fitting results of 0.65NBT-0.35SBT ceramics

Peak number	Modes	Raman shift (cm^{-1})
1	[E(LO+TO)]	111.33
2	[A_1(TO)]	248.76
3	[B_1+E(LO+TO)]	311.40
4	[E(TO)]	539.90
5	[A_1(TO')]	615.11
6	[A_1(LO)+E(TO)]	784.01

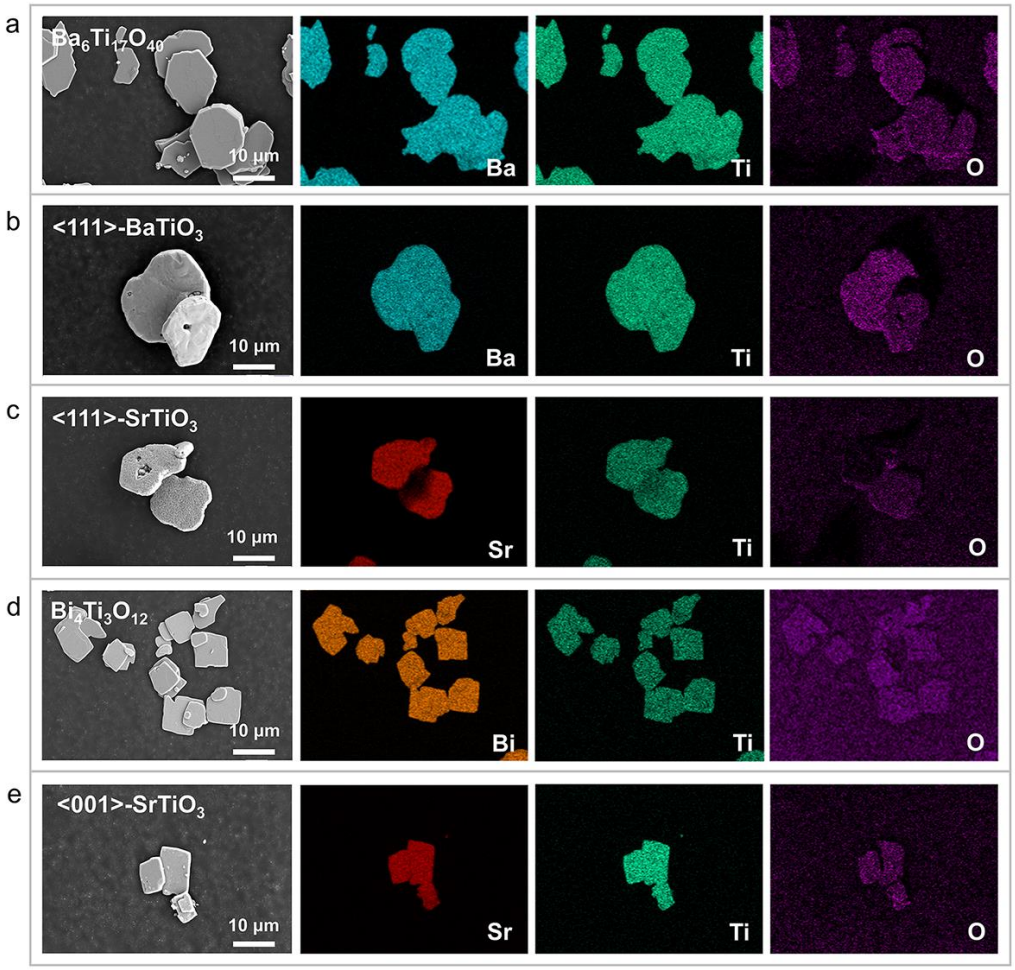

Figure S7 Surface morphology and EDS of templates and corresponding precursors: (a) $Ba_6Ti_{17}O_{40}$, (b) <111>-$BaTiO_3$, (c) <111>-$SrTiO_3$, (d)$Bi_4Ti_3O_{12}$ and (e) <001>-$SrTiO_3$

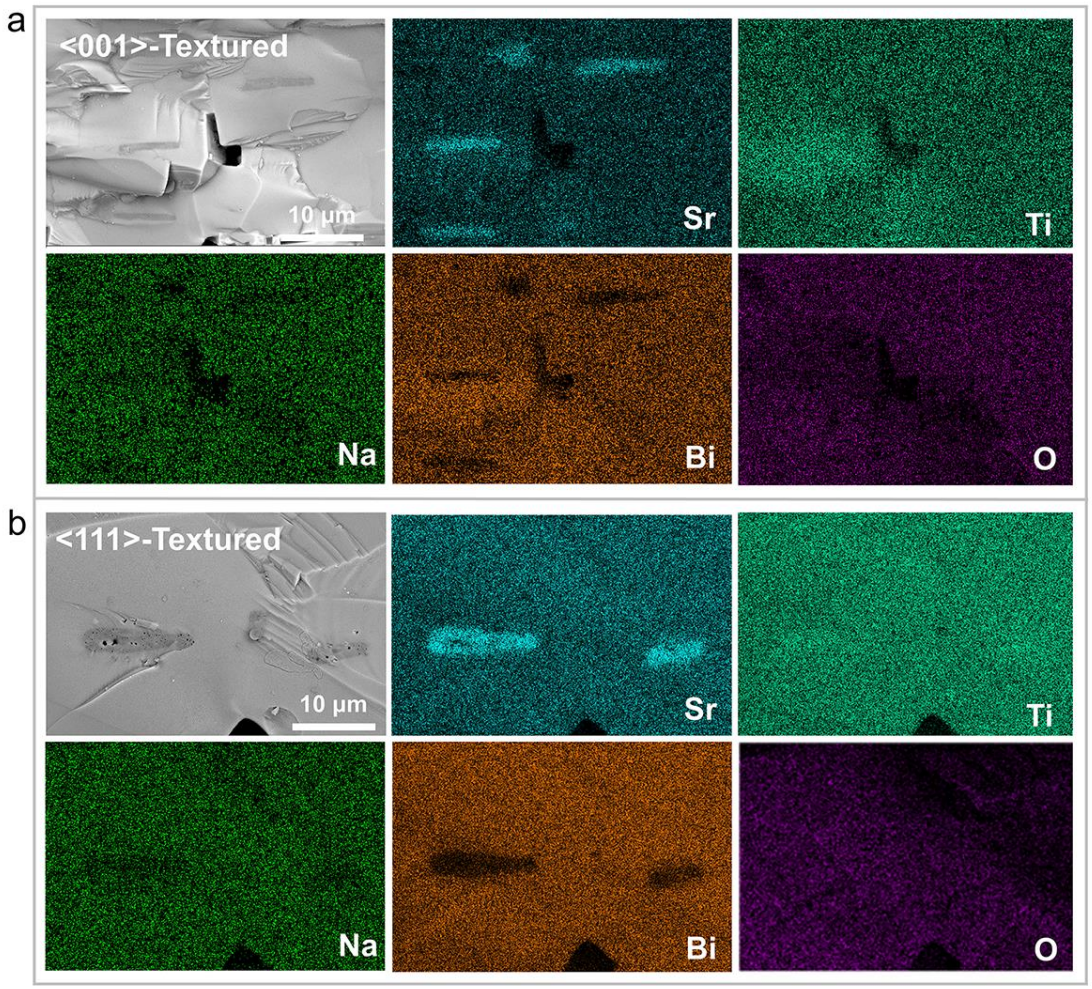

Figure S8 Grain morphology and element distribution of the cross sections of <001> and <111>-textured MLCCs

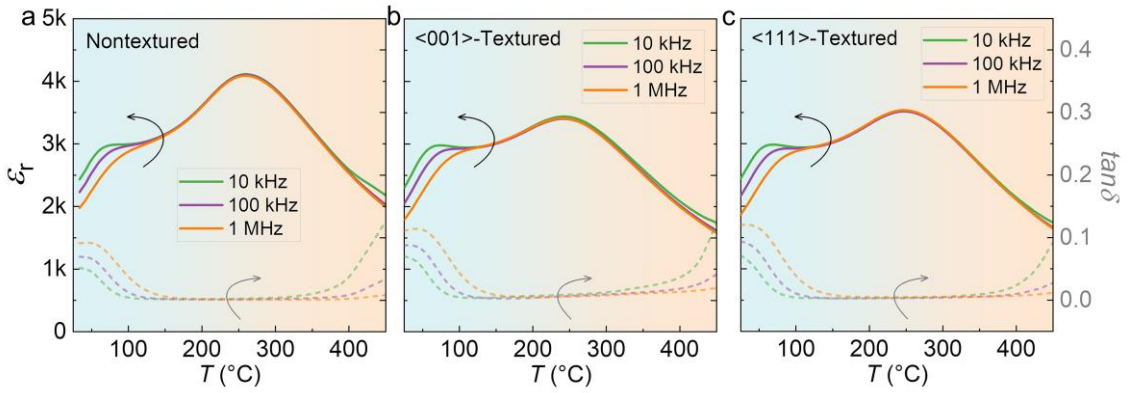

Figure S9 Dielectric temperature spectra of nontextured, <001> and <111>-textured MLCCs

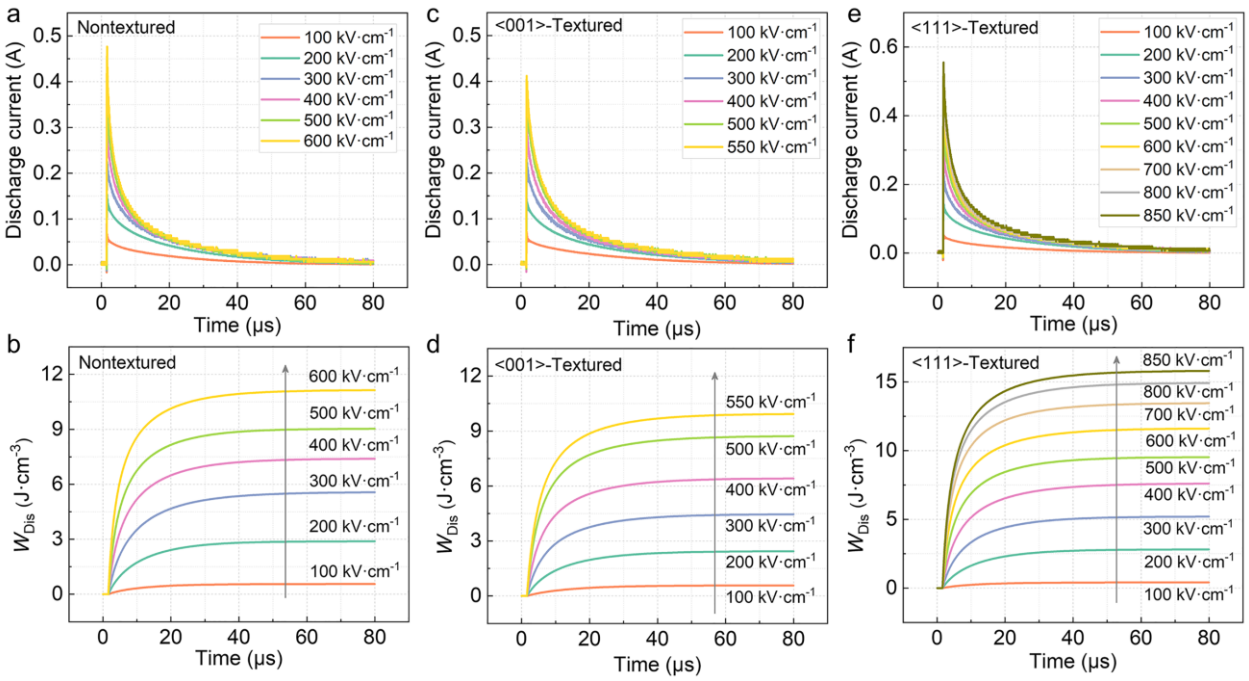

Figure S10 Pulse discharge curves and discharge energy density curves of nontextured, <001> and <111>-textured MLCCs

Table S5 Comparison of energy storage performance of dielectric ceramic materials

References	W_{rec} ($J \cdot cm^{-3}$)	η	E_B ($kV \cdot cm^{-1}$)
[1] Energy Environ. Sci. (2023)	10.28	97.11%	560
[2] Acta Mater. (2023)	14.21	87.35%	530
[3] Adv. Energy Mater. (2024)	12.65	88.5%	1100
[4] Adv. Mater. (2023)	9	84%	660
[5] Energy Stor. Mater. (2024)	8.63	89.6%	520
[6] Small (2023)	11.4	80%	670
[7] Nano Energy (2023)	6	92%	440
[8] Nat. Commun. (2023)	14	85%	1450
[9] Nano Energy (2022)	7.72	83.78%	595
[10] Adv Mater. (2022)	10.59	87.6%	550
[11] Adv Mater. (2022)	13.1	90%	740
[12] Adv. Funct. Mater. (2023)	15.1	82.4%	640
[13] Nat. Commun. (2022)	10.06	90.8%	740
[14] Nat. Commun. (2023)	9.22	96.3%	535
This work	**15.7**	**95.2%**	**850**

[1] Li, D. *et al*. A high-temperature performing and near-zero energy loss lead-free ceramic capacitor, *Energy Environ. Sci.*, **16**, 4511-4521 (2023).

[2] Yang, J. *et al*. Field-induced strain engineering to optimize antiferroelectric ceramics in breakdown strength and energy storage performance, *Acta Mater*. **257**, 119186 (2023).

[3] Lv, Z. *et al*. $NaNbO_3$-Based Multilayer Ceramic Capacitors with Ultrahigh Energy Storage Performance, *Adv. Energy Mater*. 2304291 (2024).

[4] Gao, Y. *et al*. Ultrahigh Energy Storage in Tungsten Bronze Dielectric Ceramics Through a Weakly Coupled Relaxor Design, *Adv. Mater*. 2310559 (2023).

[5] Long, C. *et al*. Excellent energy storage properties with ultrahigh W_{rec} in lead-free relaxor ferroelectrics of ternary $Bi_{0.5}Na_{0.5}TiO_3$-$SrTiO_3$-$Bi_{0.5}Li_{0.5}TiO_3$ via multiple synergistic optimization, *Energy Stor. Mater*. **65**, 103055 (2024).

[6] Chen, L. *et al*. Compromise Optimized Superior Energy Storage Performance in Lead-Free Antiferroelectrics by Antiferroelectricity Modulation and Nanodomain Engineering, *Small* 2306486 (2023).

[7] Liu, L. *et al*. Multi-scale collaborative optimization of $SrTiO_3$-based energy storage ceramics with high performance and excellent stability, *Nano Energy* **109**, 108275 (2023).

[8] Zhu, L. *et al*. Heterovalent-doping-enabled atom-displacement fluctuation leads to ultrahigh energy-storage density in $AgNbO_3$-based multilayer capacitors, *Nat. Commun*. **14**, 1166 (2023).

[9] Dong, X. *et al*. (1-*x*)[0.90NN-0.10Bi($Mg_{2/3}Nb_{1/3}$)O_3]-*x*($Bi_{0.5}Na_{0.5}$)$_{0.7}Sr_{0.3}TiO_3$ ceramics with core–shell structures: A pathway for simultaneously achieving high polarization and breakdown strength, *Nano Energy*, **101**, 107577 (2022).

[10] Chen, L. *et al*. Local Diverse Polarization Optimized Comprehensive Energy-Storage Performance in Lead-Free Superparaelectrics, *Adv. Mater*. **34**, e2205787 (2022).

[11] Xie, A. *et al*. Supercritical Relaxor Nanograined Ferroelectrics for Ultrahigh-Energy-Storage Capacitors, *Adv. Mater.* **34**, e2204356 (2022).

[12] Cao, W. *et al*. Interfacial Polarization Restriction for Ultrahigh Energy-Storage Density in Lead-Free Ceramics, *Adv. Funct. Mater*. **33**, 2301027 (2023).

[13] Chen, L. *et al*. Giant energy-storage density with ultrahigh efficiency in lead-free relaxors via high-entropy design, *Nat. Commun*. **13**, 3089 (2022).

[14] Zhao, W. *et al*. Broad-high operating temperature range and enhanced energy storage performances in lead-free ferroelectrics, *Nat. Commun*. **14**, 5725 (2023).

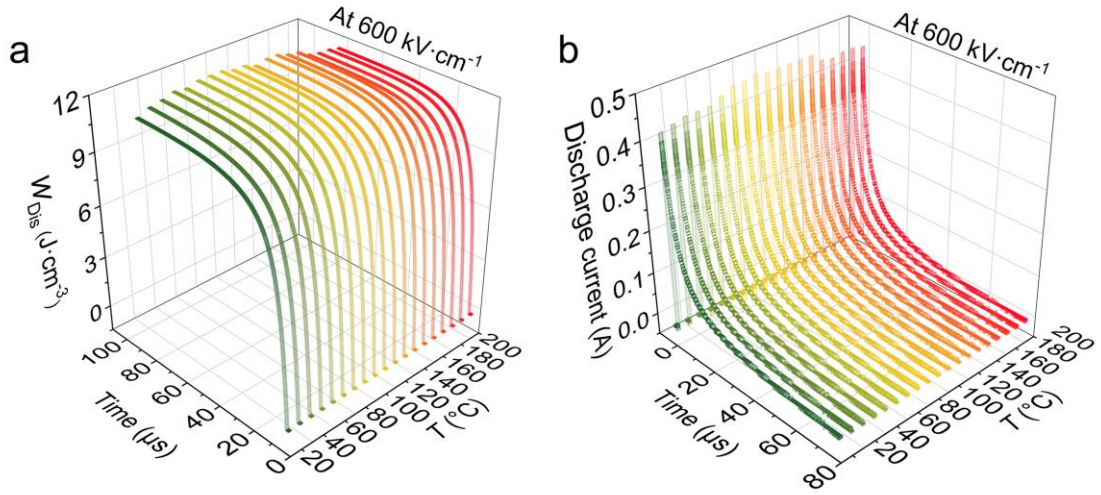

Figure S11 The pulse discharge characteristic curves of <111>-textured MLCCs in the range of 20 ~ 200 ℃